ACS Catalysis

Research Article

pubs.acs.org/acscatalysis

Dependence on Size of Supported Rh Nanoclusters in the Decomposition of Methanol

Ting-Chieh Hung,[†] Ting-Wei Liao,[†] Zhen-He Liao,[†] Po-Wei Hsu,[†] Pei-Yang Cai,[†] Hsuan Lee,[†] Yu-Ling Lai,[§] Yao-Jane Hsu,[§] Hui-Yu Chen,[‡] Jeng-Han Wang,*[,‡] and Meng-Fan Luo*[,†]

[†]Department of Physics, National Central University, 300 Jhongda Road, Jhongli 32001, Taiwan

[‡]Department of Chemistry, National Taiwan Normal University, Taipei, Taiwan

[§]National Synchrotron Radiation Research Center, 101 Hsin-Ann Road, Hsinchu Science Park, Hsinchu 30076, Taiwan

Supporting Information

ABSTRACT: The decomposition of methanol catalyzed with Rh nanoclusters supported on an ordered thin film of Al_2O_3/NiAl(100) became enhanced on decreasing the size of the clusters. The decomposition of methanol (and methanol-d_4) proceeded through dehydrogenation; the formation thereby of CO became evident above 200 K, depending little on the cluster size. In contrast, the production of CO and hydrogen (deuterium) from the reaction varied notably with the cluster size. The quantity of either CO or hydrogen produced per Rh surface site was unaltered on clusters of diameter >1.5 nm and height >0.6 nm, corresponding to about 65% of methanol undergoing decomposition on adsorption in a monolayer on the clusters. For clusters of diameter <1.5 nm and height <0.6 nm, the production per Rh surface site increased with decreasing size, up to 4 times that on the large clusters or Rh(100) single-crystal surface. The reactivity was enhanced largely because, with decreasing cluster size, the activation energy for the scission of the O−H bond in the initial dehydrogenation became smaller than the activation energy for the competing desorption. The property was associated with the edge Rh atoms at the surface of small clusters.

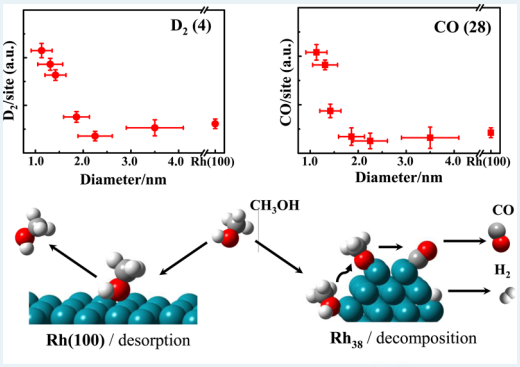

KEYWORDS: *supported Rh nanoclusters, model systems, methanol decomposition, size dependence, STM, RHEED, IRAS, TPD, PES, DFT calculations*

1. INTRODUCTION

The catalytic decomposition of methanol (CH_3OH) has been extensively investigated because the principal reaction is applied in direct methanol fuel cells (DMFCs), which offer a prospect of efficient conversion of methanol to electricity,[1−5] and because it can serve as a source of hydrogen. As the performance of DMFCs or the production of hydrogen is governed largely by the catalyzed reaction, a knowledge of the detailed reaction kinetics and a correlation between reactivity and structure of the catalysts are desirable. Many model systems, including single-crystal metallic,[6−25] alloy,[26−28] and oxide[29−32] surfaces, have been investigated to shed light on the mechanism of the reaction and to correlate reactivity with structure. The adsorption and decomposition of methanol on the surfaces of single crystals of rhodium (Rh), such as Rh(100) and Rh(111), have been studied,[33−36] as Rh catalysts have been widely used and Rh can be alloyed with catalysts based on platinum (Pt, the primary catalyst for this methanol reaction) to improve the catalytic properties. However, methanol reactions on oxide-supported Rh clusters,[37] a realistic model system, have been little investigated. Important information about the mechanism and the correlation between reactivity and structure might be lacking because of the disparity between real catalysts and single-crystal model systems. The present work has an aim to remedy this lack and to acquire insight into the detailed mechanism.

We investigated the decomposition of methanol and methanol-d_4 on Rh clusters formed on deposition of a vapor onto an ordered thin film of Al_2O_3/NiAl(100), under ultrahigh-vacuum (UHV) conditions and with various techniques to probe the surface. The morphology and structure of the Rh clusters were characterized with scanning tunneling microscopy (STM), reflection high-energy electron diffraction (RHEED), and temperature-programmed desorption (TPD); the catalyzed reactions were characterized with infrared reflection absorption spectroscopy (IRAS), TPD ,and synchrotron-based photoelectron spectroscopy (PES). These results were complemented with calculations based on density functional theory (DFT) to explore the correlation between structure and reactivity. The Rh clusters had a mean diameter from 1.0 to 3.5

Received: March 25, 2015
Revised: May 12, 2015
Published: June 4, 2015

DOI: 10.1021/acscatal.5b00579
ACS Catal. 2015, 5, 4276−4287

nm and height from 0.4 to 0.8 nm evolving with the coverage. They exhibited an fcc phase and grew with their facets (100) parallel to the θ-Al_2O_3(100) surface (denoted as Rh(100) clusters). Relative to that of bulk Rh, the lattice parameter of the structurally ordered clusters increased, up to 6% with decreasing cluster size.

Our results show that methanol on Rh clusters decomposed through only one channel—dehydrogenation to CO. The mechanism resembles that on Rh single crystals[33−35] but differs from that on supported Pt and Pd nanoclusters, for which scission of the C−O bond serves as an alternative channel.[38−40] The dehydrogenation on the Rh clusters to CO was strongly induced at a temperature above 200 K, less than that on a Rh(100) surface but similar to that on a Rh(111) surface, Ru single crystal, and supported Pt and Pd clusters.[34,35,38,40] The onset temperature varied little with cluster size, but the production of CO and hydrogen or deuterium from the reaction changed notably. The quantity of either CO or hydrogen produced per Rh surface site remained unaltered on clusters of diameter >1.5 nm and height >0.6 nm; about 65% of monolayer methanol adsorbed on the clusters decomposed, comparable to that on a Rh(100) single crystal and that on Pt clusters.[40] For clusters of diameter <1.5 nm and height <0.6 nm, the production increased significantly with decreasing cluster size; at a cluster diameter near 1.0 nm and height near 0.4 nm, the production of CO and hydrogen per Rh surface site is 4 times that on large clusters or a Rh(100) surface. An analogous reactivity dependent on size was not observed on systems such as supported Pt and Pd clusters.[38−40] Small Rh clusters hence possess two superior catalytic properties—great reactivity toward the dehydrogenation of methanol and little poisoning effect of elemental carbon remaining from the reaction.[41−43] Our DFT calculations show that the path of dehydrogenation through scission of first O−H and then C−H bonds was energetically favored on both small and large clusters; the size-dependent activation energies for scission of the O−H bond and for desorption of methanol largely accounted for the increased reactivity.

2. METHODS

2.1. Experimental Details. Our experiments were performed in UHV chambers with a base pressure in a 10^{-10} Torr regime. A NiAl(100) sample (MaTeck GmbH) was polished to a roughness of less than 30 nm and an orientation accuracy better than 0.1°; a Rh(100) sample (MaTeck GmbH) was polished to an orientation accuracy better than 1°. To obtain a clean surface, the sample underwent alternative cycles of sputtering and subsequent annealing before each experiment. The cleanliness of the sample was monitored with Auger electron spectroscopy, low-energy electron diffraction, and STM. An ultrathin θ-Al_2O_3 film was formed on oxidation of a NiAl(100) alloy surface at 1000 K; the formation of Al_2O_3 thin films is described elsewhere.[44−47] To achieve a homogeneous crystalline Al_2O_3 surface with no NiAl facets,[48,49] we refrained from protracted postoxidation annealing of the oxide films. The amorphous oxide surface was also negligible. The grown θ-Al_2O_3 thin film had a thickness of 0.5−1.0 nm.[44,47] The sample was then quenched to 300 K for vapor deposition of Rh from an ultrapure Rh rod heated by electron bombardment in a commercial evaporator (Omicron EFM 3). The rate of deposition of Rh was fixed at about 0.15 ML/min, calculated according to the coverage prepared at 300 K. The coverage was estimated from the volume of the Rh clusters observed with STM; 1.0 ML corresponds to a density of 1.39×10^{15} atoms/cm^2 of fcc Rh(100) surface atoms. After the deposition, the sample was cooled to the desired adsorption temperature (100 K, unless specified). Methanol and CO gas were dosed by a doser pointing to the sample, with a background pressure of $(2-5) \times 10^{-9}$ Torr. The highly pure methanol and methanol-d_4 (Merck, 99.8%) were additionally purified by repeated freeze−pump−thaw cycles. We report methanol and CO exposures in Langmuir units (1.0 L = 10^{-6} Torr s).

STM images (recorded with a RHK UHV 300 unit), constant-current topographies, were obtained at 90 K with a sample bias voltage of typically 2.4−2.8 V and a tunneling current of 0.8−1.2 nA. The STM tip consisted of an electrochemically etched tungsten wire. RHEED was performed with an incident electron beam of energy 40 keV at a grazing angle of 2−3° to the surface. TPD spectra were taken by ramping the sample at 3 K/s and monitoring the various masses on a quadruple mass spectrometer (Hiden), which was shielded and placed close (about 2 mm) to the sample. IRAS spectra were collected using a Fourier transform infrared spectrometer (FTLA 2000) with external optics aligned for an incident angle 75° from the sample normal, and a liquid-nitrogen-cooled MCT detector. The IRAS spectra are presented as the ratio of sample and oxide surface (or Rh cluster) data measured at the same surface temperature (100 K) and are typically the average of 256 scans at resolution 4 cm^{-1}. The PES experiments were performed at the U5-spectroscopy beamline at the National Synchrotron Radiation Research Center in Taiwan.[50] The energy resolution was estimated to be near 0.1 eV. The photon energies were fixed at 383 eV. The beam was incident normal to the surface; photoelectrons were collected at angle of 58° from the surface normal. All photoelectron spectra presented here were first normalized to the photon flux. The binding energy (BE) is referred to the substrate bulk Al 2p core level at 72.9 eV.[51−53]

2.2. Computational Method. The calculations were performed using the Vienna ab initio simulation package (VASP),[54−56] at the density functional theory (DFT) level with a 3D periodic boundary condition. The exchange-correlation function was treated by the generalized gradient approximation[57] with the Perdew−Wang 1991 formulation (GGA-PW91).[58] The electron−ion interaction was modeled by the projector-augmented wave method (PAW),[59,60] combining the accuracy of augmented plane waves with cost-effective pseudopotentials. The kinetic cutoff energy of the plane-wave basis was set at 600 eV. The Brillouin zone (BZ) integration was sampled by the Monkhorst−Pack scheme[61] at a 0.05 × 2 (1/Å) interval in the reciprocal space. All of the modeled clusters, surfaces, and related adsorptions were optimized by a quasi-Newton method with an energetic convergence of 1×10^{-4} eV and a gradient convergence of 1×10^{-2} eV. The minimum energy path and the corresponding activation energy for each step were calculated using the nudged elastic band (NEB) method[62] at the same energetic and gradient convergences.

3. RESULTS

3.1. Morphology and Structure of Supported Rh Clusters. The growth of Rh clusters from deposition of a vapor on Al_2O_3/NiAl(100) at 300 K was characterized primarily with STM and RHEED. Figure 1a−d exemplifies morphologies and sizes of Rh clusters at varied coverages on Al_2O_3/NiAl(100); Figure 1e−g plots the evolution of the mean diameter, height,

DOI: 10.1021/acscatal.5b00579
ACS Catal. 2015, 5, 4276−4287

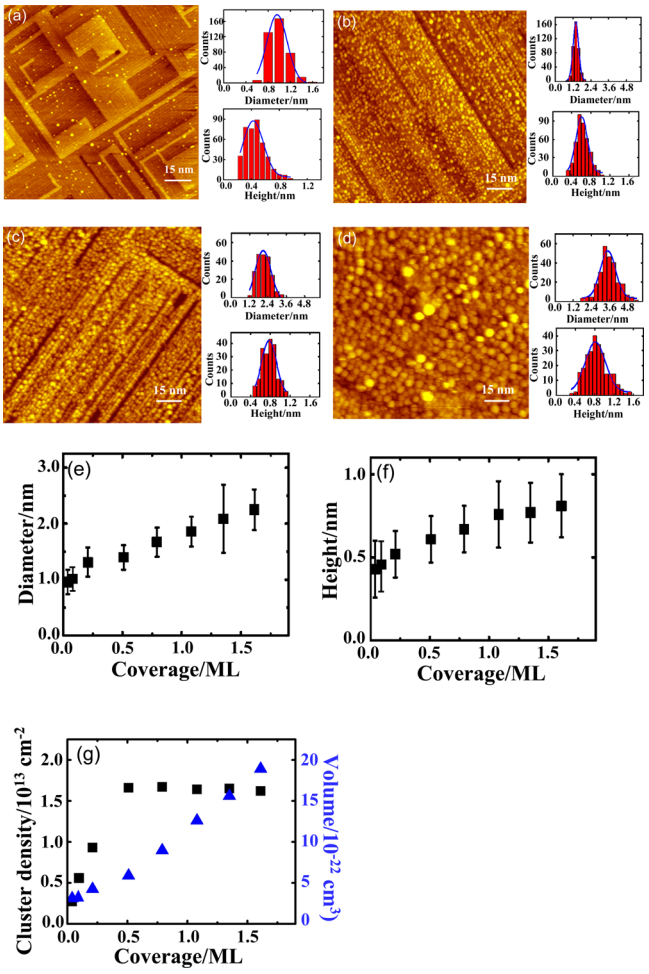

Figure 1. (a–d) STM images for 0.05, 0.5, 1.35, and 4.0 ML Rh deposited on a thin film of Al_2O_3/NiAl(100) at 300 K. The insets parts a–d show characteristic histograms of height and diameter for each coverage; the curves are the best Gaussian fits to the distributions. (e–g) Plots of the evolution of the mean diameter, height, and density, respectively, of Rh clusters with the coverage. The errors bars in parts e and f indicate the full width at half-maximum of the best Gaussian fits to the histograms of diameter and height of Rh clusters for each coverage. The triangles in part g show mean volumes of individual clusters at varied Rh coverages, estimated from the mean diameter and height.

and density of Rh clusters with coverage. The insets in Figure 1a–d show characteristic histograms of the height and diameter for each coverage; the curve in each histogram is a Gaussian fit to the size distribution. The error bars in Figure 1e,f indicate the full width at half-maximum of the best Gaussian fits to the distributions of diameter and height of the clusters for each coverage. At the least coverage, 0.05 ML (Figure 1a), the clusters had a mean diameter of about 1.0 nm and height of about 0.4 nm; when coverage was increased to 0.5 (1.35) ML, the mean diameter and height increased to 1.4 (2.0) and 0.6 (0.8) nm, respectively (Figure 1b,c). The size—diameter, height, and volume—of the clusters continued to increase with increasing coverage, plotted in Figure 1e–g. The cluster density increased initially with the Rh deposition but was saturated at about 0.5 ML (black squares, Figure 1g), above which further deposited Rh joined existing clusters instead of forming new clusters. At a coverage of greater than 2.0 ML, the clusters generally coalesced. At 4.0 ML (Figure 1d), the diameter of Rh clusters increased to 3.5 nm but the height altered little. The size was not measured accurately at this stage, as the lower portions of the clusters became merged and thin films formed. The images also show that most Rh grew along stripe protrusions of crystalline Al_2O_3/NiAl(100) (Figure 1a–c), which were the sites favored for nucleation.[48,63] This observation indicates that diffusion of Rh atoms was efficient on the surface at 300 K; the diffusion remained efficient even at 150 K, as clusters grown at 150 and 300 K had comparable sizes. This feature is consistent with that previously observed for Rh clusters on Al_2O_3/NiAl(110).[42,64] The thermal stability of the Rh clusters was also examined. For small clusters (≤0.5 ML), the size altered little with the annealing temperature (≤800 K), despite a decrease in the cluster density above 500 K; for large clusters (≥1.0 ML), the diameter changed above 430 K but the height remained unchanged with the annealing temperature (≤800 K).

The structural ordering of the Rh clusters is reflected in the RHEED patterns shown in Figure 2a–d. The reflection rods of

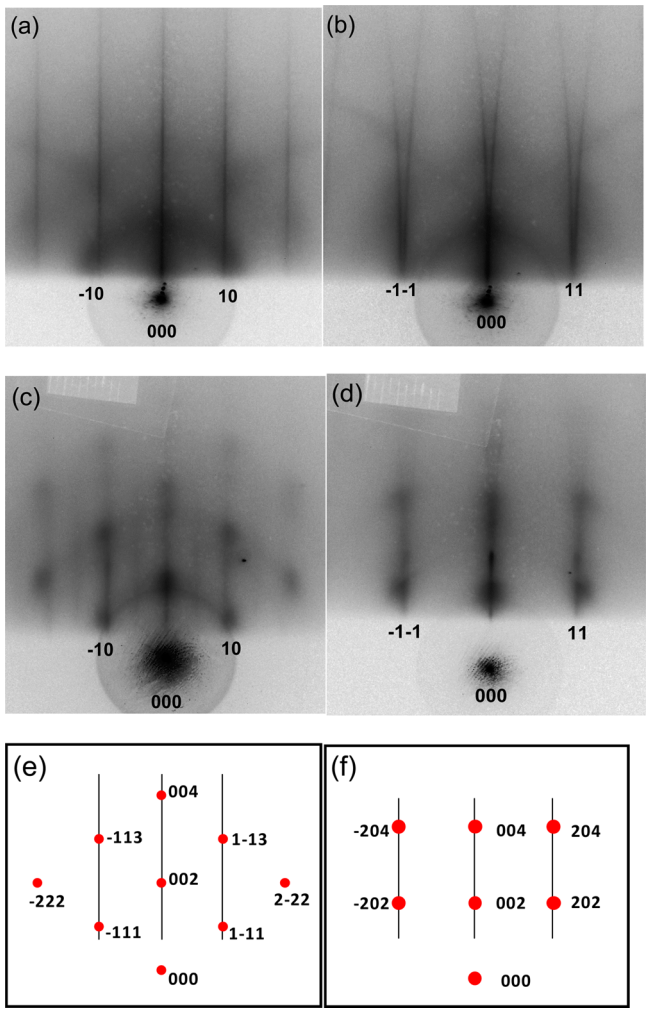

Figure 2. RHEED patterns for 1.0 and 3.0 ML Rh deposited on Al_2O_3/NiAl(100) at 300 K. Parts a and b show patterns obtained from 1.0 ML Rh clusters at azimuths [0–10] and [0–11], respectively, and parts c and d show patterns obtained from 3.0 ML Rh clusters at azimuths [0–10] and [0–11], respectively. Parts e and f show schematic reciprocal-lattice nets in the incident directions [0–10] and [0–11], respectively. Red spots in parts e and f denote reciprocal-lattice points for the clusters of Rh(001)[110]//Al_2O_3(100)[010].

DOI: 10.1021/acscatal.5b00579
ACS Catal. 2015, 5, 4276–4287

the RHEED patterns in the figures are ascribed to the oxide and the NiAl(100) substrate; upon deposition of Rh, the half-order reflections from the (2 × 1) structure of ordered θ-Al_2O_3(100)[44−47] either disappeared (Figure 2a) or became vague (Figure 2c). Additional patterns superimposed on the reflection rods at azimuths [0−10] and [0−11] resulted from structurally ordered Rh clusters. The patterns were evident at 1.0 ML (Figure 2a,b) and became even sharper with increasing coverage (Figure 2c,d). The trend implies that the content of the ordered structures increased in larger clusters. The structurally ordered clusters had an fcc phase and grew preferentially with their (100) facets parallel to the θ-Al_2O_3(100) surface; their [110] axes lay along direction [010] of the oxide surface: thus, Rh(100)[110]//Al_2O_3(100)-[010]. The corresponding points of the reciprocal lattice at the two azimuths are plotted schematically in Figure 2e,f. This orientation is preferred because the (100) facets of the Rh clusters are a better structural match for the square oxygen lattice of the θ-Al_2O_3(100) surface,[65−67] as illustrated in Figure 3a. The lattice parameters of the Rh clusters also increased to match the oxide surface. The Rh clusters of diameter near 1.8 nm and height near 0.7 nm (1.0 ML) had a mean lattice parameter of about 4.04 Å, increased by about 6% with respect to bulk Rh (3.80 Å). The expansion decreased with increasing size or coverage (plotted in Figure 3b), as the substrate effect on the upper layers of the growing clusters attenuated. A similar substrate effect was previously shown for Rh nanoclusters on a graphene template, for which the lattice parameter of Rh clusters decreased to match the graphene surface.[68] For a coverage at or smaller than 0.5 ML, no clear diffraction pattern was observed for the clusters (diameter ≤1.5 nm and height ≤0.6 nm). The (100) orientation is expected to be retained for small clusters. No clear diffraction pattern was shown because the content of the ordered structures decreased in small clusters.

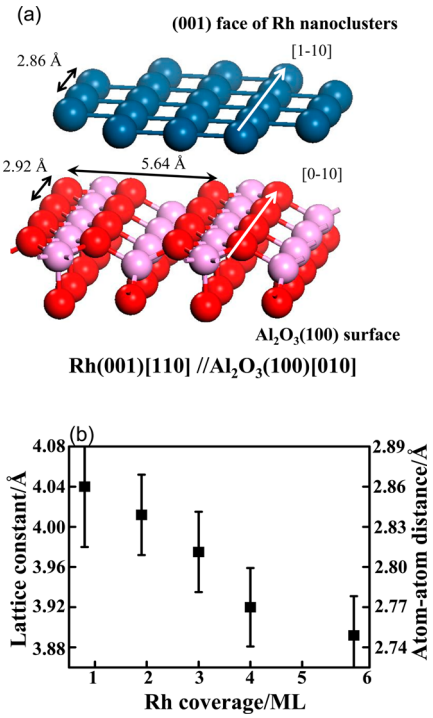

Figure 3. (a) Schematic diagram illustrating the growth of fcc Rh clusters in the (001) orientation (top), with respect to the θ-Al_2O_3 (100) surface (bottom). (b) Lattice parameters of Rh clusters as a function of Rh coverage. In part a, blue, red, and purple balls denote Rh, oxygen and aluminum atoms, respectively. The interatomic distance, 2.86 Å, is indicated for the Rh clusters (at 1.0 ML). The diagram of the (100) oxide surface in part a is drawn according to refs 44 and 46; the lattice parameters given are from the same references. The lattice parameters were determined by fitting the reciprocal-lattice nets to the brightest areas of the diffraction pattern (top 2% in intensity). The error bars are given on the basis of the reproducibility and size of the brightest areas.

3.2. Characterization of Decomposition of Methanol or Methanol-d_4 on Rh Clusters. The reactions of methanol and methanol-d_4 on the supported Rh clusters were characterized with TPD, IRAS, and PES. Adsorbed methanol and methanol-d_4 showed similar desorption behavior, but the latter gave clearer D_2 signals in comparison to the signals for H_2. Methanol-d_4 was hence used for the series of TPD experiments. Figure 4 exemplifies the TPD spectra of methanol-d_4 (CD_3OD), CO, D_2, and CD_4 for Rh clusters (1.0 ML) on Al_2O_3/NiAl(100) exposed to CD_3OD (2.0 L). The desorption of CD_3OD (top of Figure 4) exhibited two distinct features. The greater feature, between 110 and 170 K, is attributed primarily to the desorption of multilayer methanol-d_4, as the feature was never saturated and was observed on varied surfaces.[6,11,12,40,69] The desorption of monolayer methanol-d_4 on the Rh clusters also contributed to the feature, given that the monolayer methanol-d_4 on the Rh(100) surface desorbed at about 160 K.[35] The other with a maximum at about 200 K and extending to 270 K was due primarily to the desorption of monolayer methanol-d_4 on the uncovered alumina film. Monolayer methanol-d_4 on pristine Al_2O_3/NiAl(100) desorbed in the same temperature regime.[69] The desorbing CD_3OD gave cracking patterns in the CO and D_2 spectra (second and third in Figure 4) in the corresponding temperature range. The CD_4 signals (fourth in Figure 4) in this temperature range resulted largely from the background, as these signals also appeared for methanol-d_4 adsorbed on the oxide. The CO and D_2 desorption signals at temperatures >200 K were from dehydrogenated methanol-d_4. A lack of CD_4 signal

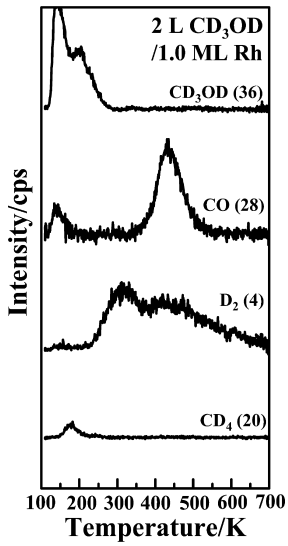

Figure 4. TPD spectra of CD_3OD (m/z 36), CO (m/z 28), D_2 (m/z 4), and CD_4 (m/z 20) from 2.0 L of CD_3OD adsorbed at 100 K on 1.0 ML Rh clusters/Al_2O_3/NiAl(100). Rh was deposited at 300 K.

DOI: 10.1021/acscatal.5b00579
ACS Catal. 2015, 5, 4276−4287

indicates that the alternative channel, scission of the C−O bond in methanol-d_4, did not open in this reaction. No signal of CD_2O (m/z 20) was observed, other than the cracking pattern of desorbing methanol-d_4 in the CD_2O spectra (not shown). Formaldehyde as an intermediate was unstable, as it decomposed further rather than desorbing. As no desorption of CO, D_2, or CD_4, except the methanol-d_4-cracking pattern and background, was observed for methanol-d_4 on Al_2O_3/NiAl(100),[40] the decomposition must have occurred on the clusters. The Al_2O_3/NiAl(100) support was not involved in the reaction. Intermediates and the final products from decomposed methanol-d_4 were not observed to migrate to or desorb from Al_2O_3/NiAl(100). The chemically inert property resembles that of typical alumina supports.

The CO produced from dehydrogenated methanol-d_4 (denoted as CO_m) desorbed above 350 K; the desorption continued to about 540 K. This desorption range is similar to that from Rh single crystals[33−35] and similar also to that of molecularly adsorbed CO on Rh clusters (Figure 5).[70,71] None of the CO_m desorbed from the Al_2O_3/NiAl(100) surface, since the adsorption temperature for CO on Al_2O_3/NiAl(100) is below 100 K. As adsorbed methanol-d_4 decomposed to CO_m far below 350 K (indicated by the IRAS, below), CO_m moved to preferred sites and desorbed as molecularly adsorbed CO. D_2, from dehydrogenated methanol-d_4, desorbed above 250 K; the desorption extended to about 700 K. The D_2 spectra clearly exhibited two features: one had a maximum about 320 K, and the other was centered about 450 K and extended to 700 K. The feature at a temperature of >450 K was not observed in the spectra of H_2 desorption of either dehydrogenated methanol or atomically adsorbed hydrogen (H) on the Rh clusters. We attribute the difference to an isotopic effect on the recombinative desorption of H (or D) atoms. A comparison of D_2 and H_2 spectra from dehydrogenated methanol-d_4, methanol, and adsorbed atomic hydrogen is presented in the Supporting Information.

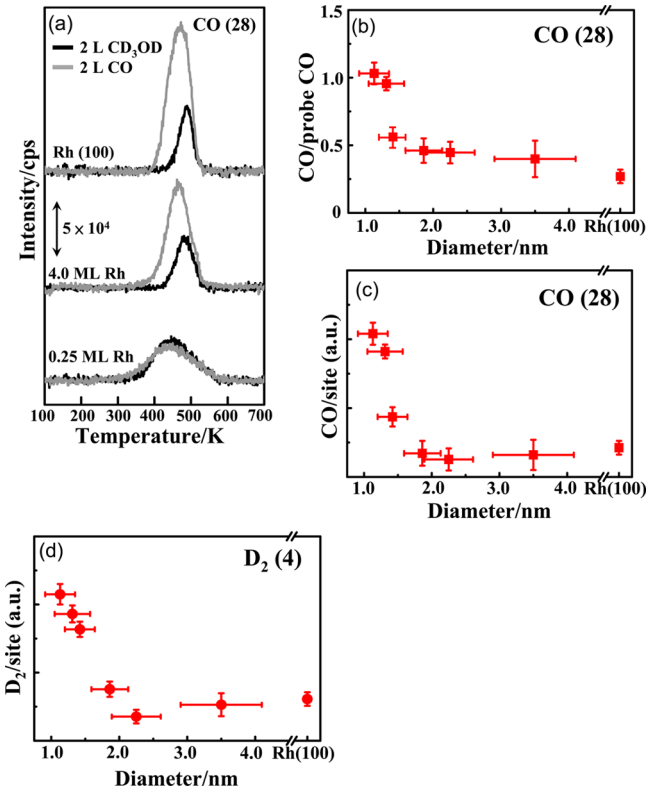

Figure 5. (a) CO TPD spectra for 2.0 L of CD_3OD (black) and 2.0 L of CO (gray) molecularly adsorbed on a Rh(100) single crystal and 4.0 and 0.25 ML Rh clusters on Al_2O_3/NiAl(100) at 100 K. (b) Ratio of integrated intensities of CO TPD spectra from 2.0 L of CD_3OD and 2.0 L of CO on Rh clusters as a function of cluster diameter, (c, d) Production of CO_m and D_2 per surface Rh site (from 2.0 L of CD_3OD) as a function of cluster diameter. In parts c and d, the quantities of the produced CO_m and D_2 were measured as the integrated intensities of CO and D_2 TPD spectra and the number of surface Rh sites by the surface area of the Rh clusters measured with STM. The sizes in parts b−-d correspond to Rh clusters at 0.13, 0.25, 0.5, 1.0, 1.6, and 4.0 ML. Rh was deposited at 300 K.

The quantities of CO_m and D_2 produced from decomposed methanol-d_4 manifest that the reactivity of the Rh clusters depended on their size. Figure 5a compares the CO TPD spectra of molecularly adsorbed CO and CO_m on a Rh(100) single crystal and on Rh clusters. The molecularly adsorbed CO was prepared on exposing the sample to 2.0 L of CO at 100 K; CO_m was produced from 2.0 L of methanol-d_4 adsorbed on the samples, for which a multilayer of methanol-d_4 already formed. For a Rh(100) single crystal (top spectrum), the integrated intensity of desorption of CO_m (black) was about one-fourth that of molecularly adsorbed CO (gray). The onset temperatures of desorption of CO and CO_m differed because CO_m saturated the cluster surface much less than CO. The fraction increased slightly to 35% for 4.0 ML Rh clusters (middle spectrum) but greatly to 1.0 for 0.25 ML Rh clusters (third spectrum). As the size of the clusters decreased with decreasing coverage (Figure 1) and as the desorption intensity of molecularly adsorbed CO served as a rough measure of the number of surface Rh sites, the result indicates that the production of CO_m per surface site, corresponding to the reactivity, was enhanced on the small Rh clusters. Figure 5b plots the ratio of the desorption intensities of CO_m and molecularly adsorbed CO as a function of cluster diameter. The ratio varied little for a diameter >1.5 nm but increased notably for a diameter <1.5 nm. To corroborate the results, we also estimated the number of surface sites with the surface area of the Rh clusters measured with STM. The estimate, which complements the above TPD approach,[72,73] shows a consistent trend: the production of either CO_m or D_2 per surface site increased significantly for a cluster diameter <1.5 nm (Figure 5c,d). The measured signals for CO_m desorption were not for all CO_m produced on the surface, as a fraction of surface CO_m dissociated rather than desorbing. The rate of dissociation varied with the cluster size,[41−43] but altered little the production trend, as the trends for CO_m and D_2 were so similar (Figure 5c,d). The production of CO_m or D_2 per Rh surface site on the clusters of diameter about 1.0 nm and height about 0.4 nm (0.05 ML Rh) was nearly 4 times that on clusters of diameter >1.5 nm and height >0.6 nm (>0.5 ML Rh) or the Rh(100) surface. These results imply that we can control the reactivity of the supported Rh clusters by tuning their size.

The probability of dehydrogenation of methanol adsorbed on Rh clusters was derived by combining the TPD with PES spectra of methanol-d_4 (methanol) and CO_m. Figure 6 shows TPD spectra of CD_3OD from 4.0 ML Rh clusters/Al_2O_3/NiAl(100), a Rh(100) single crystal, and a pristine thin film of Al_2O_3/NiAl(100). All spectra show a distinct feature between 110 and 150 K, attributed to desorption of multilayer methanol-d_4. The spectra from a Rh(100) single crystal and from Al_2O_3/NiAl(100) clearly exhibit separate maxima

DOI: 10.1021/acscatal.5b00579
ACS Catal. 2015, 5, 4276−4287

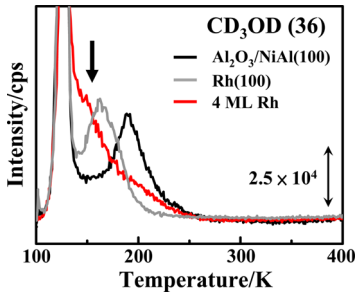

Figure 6. TPD spectra of CD_3OD (m/z 36) from 2.0 L of CD_3OD adsorbed on a pristine thin film of Al_2O_3/NiAl(100), Rh(100) single crystal, and 4.0 ML Rh clusters on Al_2O_3/NiAl(100) at 100 K. The Rh clusters were grown at 300 K.

centered at about 160 K (gray) and 190 K (black), respectively, assigned to monolayer methanol-d_4 on the two surfaces.[35,69] In contrast, the spectrum from 4.0 ML Rh clusters shows no such separate maximum from the desorption of multilayer methanol-d_4, but a shoulder extending from 150 to 270 K (red). As 4.0 ML Rh clusters covered the entire oxide surface (Figure 1d), the shoulder is ascribed to monolayer methanol-d_4 desorbing from the Rh clusters. The integrated intensity of the desorption of monolayer methanol-d_4 reflects the amount of adsorbed methanol-d_4 that did not react; that of CO_m measures the amount of reacting methanol-d_4.[74] With these desorption data and the known rate of dissociation of CO_m,[75] we derived the probability of monolayer methanol-d_4 undergoing dehydrogenation to be 65 ± 5% on 4.0 ML Rh clusters and 63 ± 2% on a Rh(100) single crystal. The similar values agree with their reactivities (Figure 5b−-d). As the production of CO_m and D_2 per surface site on clusters with <0.5 ML Rh is 2−4 times that on 4.0 ML Rh clusters (Figure 5), the probability of dehydrogenation on the small clusters must have attained nearly unity, and more methanol-d_4 molecules must have reacted on each Rh surface site. A detailed discussion of the mechanism is given in the following section.

We performed CO IRAS experiments to explore the activation energy for the dehydrogenation of methanol to CO_m on the Rh clusters. The process was evidently activated above 200 K and varied little with cluster size. Figure 7a,b presents the CO IRAS spectra for methanol on Rh clusters at sizes of 0.5 and 4.0 ML Rh. For the smaller Rh clusters (Figure 7a), no C−O stretching (ν_{CO}) signals of CO_m were observed when the sample was exposed to methanol at 100 K (top). On annealing to 200 K, an absorption line appeared near 1990 cm^{-1}, indicating that CO_m formed from dehydrogenated methanol and adsorbed on an atop Rh site.[73,76−78] With an increase in temperature, the absorption and the wavenumber increased as the dehydrogenation continued and produced more CO_m. At 350 K, the intensity attained a maximum and the wavenumber increased to about 2035 cm^{-1}. Elevating the temperature further above 400 K decreased the intensity, because CO_m either desorbed or dissociated. For the larger Rh clusters (Figure 7b), the trend was similar. The top curve in Figure tthatb from the Rh clusters before methanol adsorption shows two small absorption features at about 2000 and 1880 cm^{-1}, ascribed to contaminative CO on Rh at atop and bridge (and/or hollow)[76−78] sites, respectively. In the present work the adsorption of CO (or CO_m) at bridge or hollow sites occurred only on large clusters. Upon adsorption of methanol, the CO features broadened and shifted negatively (the second

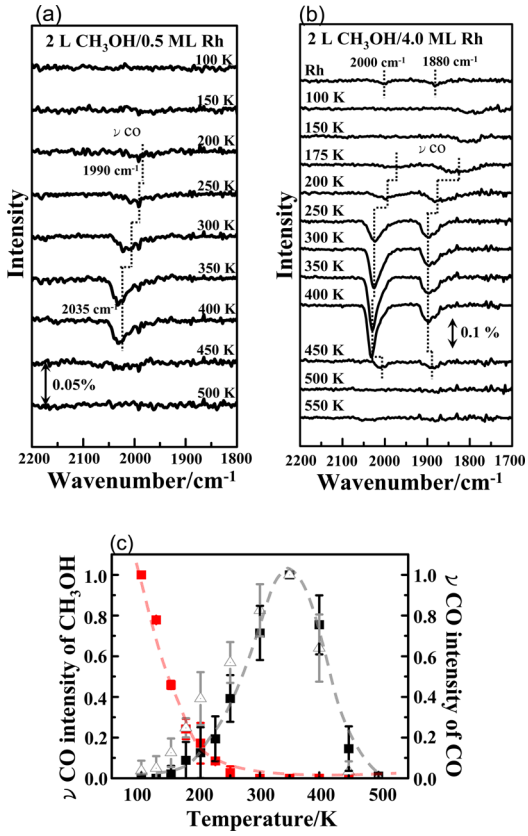

Figure 7. CO IRAS spectra from 2.0 L of CH_3OH adsorbed on (a) 0.5 ML and (b) 4.0 ML Rh clusters on Al_2O_3/NiAl(100) at 100 K and annealed to selected temperatures. (c) Integrated intensities of C−O stretching absorption (ν_{CO}) for CO (black squares and gray triangles) and CH_3OH (red squares) as a function of temperature. Rh clusters were formed at 300 K; each spectrum was recorded when the surface was cooled to about 100 K after annealing to the indicated temperature. For part c, the error bars indicate reproducibility; both red and black squares were based on the results of the Rh coverages 0.25 and 0.5 ML and triangles on the results of coverages 1.0, 1.6, and 4.0 ML. The CO intensities obtained for any Rh coverage were normalized to the maximum one (350 K); the ν_{CO} intensities of methanol were normalized to that at 100 K.

curve in Figure 7b), because of the coadsorbed methanol. The same effect was reported for CO coadsorbed with methanol on Au and Pt clusters.[40,69] On annealing to 175 and 200 K, as methanol desorbed and the effect of coadsorbed methanol decreased, the CO lines were restored to some extent: both the wavenumber and intensity increased. The integrated intensity of the CO line at 175 K exceeded that from contaminative CO (top), implying the onset of dehydrogenation of methanol to CO_m. Like the observation on the smaller clusters, the CO_m signals continued to increase with a further increase in temperature. The signals of CO_m at atop and bridge sites increased up to 350 and 250 K, respectively. A blue shift for the CO_m signals reflecting adsorption on oxidized Rh[79−81] was not observed on either small or large Rh clusters at varied temperatures. Similar results were shown for molecularly adsorbed CO. Figure 7c plots the variation with temperature of the intensity of the C−O stretching absorption for CO_m (relative to the CO contamination level) on both small (black squares) and large clusters (empty triangles). The error bars indicate reproducibility, on the basis of results for varied Rh coverages. Similar variations were shown for both small and

DOI: 10.1021/acscatal.5b00579
ACS Catal. 2015, 5, 4276−4287

large clusters: CO_m was produced strongly above 200 K, and the quantity attained a maximum at 350 K. The similarity reflects comparable activation energies for the crucial step of dehydrogenation to CO_m on small and large clusters. This crucial step accounts little for the enhanced reactivity. The IRAS measurements also suggest that the dehydrogenation was complete about 350 K, at which the cluster sizes and morphologies remained unaltered. The size−production correlation established in Figure 5 is thus robust.

The C−O stretching and C−H and O−H absorption lines in IRAS spectra for methanol were also recorded. These absorption modes decreased with an increase in temperature, reflecting the desorption and dehydrogenation of adsorbed methanol. The temperature-dependent variation of intensity of the C−O stretching mode of methanol (red squares) is plotted as a contrast to that of CO_m. The C−O stretching signals at elevated temperature were partially contributed by the intermediate methoxy, as on Rh single crystals the methoxy line formed at 140−225 K and gave vibrational features scarcely distinct from those of methanol.[34,35] Consistent with the desorption experiments and the CO IRAS spectra, the C−O stretching signals vanished at 250−300 K. No feature of formaldehyde was observed in our IRAS spectra. Examples of these spectra are presented in the Supporting Information.

From another aspect, our PES spectra provide information about the formation and dissociation of CO_m. Figure 8a shows

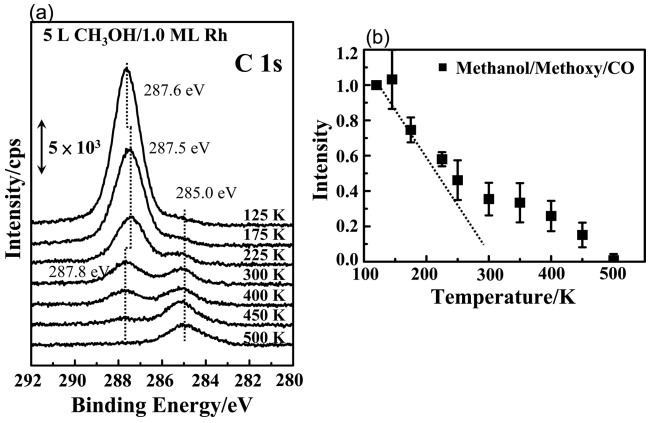

Figure 8. (a) C 1s photoelectron spectra from 5.0 L of CH_3OH adsorbed on 1.0 ML Rh clusters on Al_2O_3/NiAl(100) at 125 K and annealed to selected temperatures. (b) Integrated intensities of C 1s spectra for methanol/methoxy/CO as a function of temperature. The Rh clusters were formed at 300 K, and each spectrum was recorded when the surface was cooled to about 125 K after annealing to the indicated temperature. For part b, the error bars indicate reproducibility, on the basis of results of varied Rh coverage (0.5, 1.0, and 3.0 ML). The intensity of the C 1s line for methanol/methoxy/CO obtained from any Rh coverage was normalized to that at 125 K.

the C 1s PES spectra from 5.0 L of methanol adsorbed on 1.0 ML Rh clusters/Al_2O_3/NiAl(100) and annealed to selected temperatures. The line initially centered at about BE 287.6 eV is assigned to C 1s of methanol on Rh clusters and on Al_2O_3/NiAl(100); the feature at about 285.0 eV is assigned to C 1s of contaminative elemental carbon. On an increase in the temperature to 175 and 225 K, methanol desorbed or decomposed; the remaining methanol, CO_m, and methoxy on the Rh sites gave an attenuated C 1s line at about BE 287.6 eV. As CO on the Rh clusters yielded C 1s signals at BE 287.0−287.5 eV[42,43] and methoxy near the C 1s signals of methanol,[25] the line position altered little. On annealing above 300 K, the C 1s line at 287.5 eV continued to decrease and shifted positively to 287.8 eV. This effect did not depend on coverage, as the corresponding C 1s signals shifted negatively to smaller BE with decreasing coverage of either methanol or CO. The atypical positive shift is also not attributed to methanol adsorbed on Al_2O_3/NiAl(100),[66] as the same result was observed on 3.0 ML Rh clusters/Al_2O_3/NiAl(100), for which the oxide surface was entirely covered with Rh. At temperatures >300 K, few methanol and methoxy molecules remained (Figure 7c and the Supporting Information) and no formaldehyde was indicated. The C 1s signal of methoxy is expected at a smaller BE value,[25] and formaldehyde on Rh was shown to decompose to CO at 130 K.[34,82] The signals are assigned to CO_m, and the shift resulted from CO_m coexisting with atomic oxygen from dissociation of CO_m or with hydroxyl formed on combination of atomic oxygen and hydrogen from dehydrogenated methanol. As CO_m might interact with atomic oxygen or with hydroxyl, the C 1s signals shifted to a BE value nearer that for the carboxyl (−COOH) group.[83−85] The dissociation of CO_m became evident above 300 K, reflecting the apparently increased C 1s signals of elemental carbon.[42,43] The C 1s signals of CO_m vanished at about 500 K through dissociation and desorption, consistent with the above TPD and IRAS spectra. The same features were observed for other Rh coverages. We plotted the variation of C 1s integrated intensities of methanol/methoxy/CO_m as a function of temperature (Figure 8b); the error bars indicate the reproducibility, on the basis of the results from methanol on 0.5, 1.0, and 3.0 ML Rh clusters/Al_2O_3/NiAl(100). The C 1s intensity shows two decreasing behaviors with an increase in temperature: the rate decreased more at 125−225 K than at 225−500 K. The former reflects the desorption of methanol and the latter primarily the desorption and dissociation of CO_m. These results indicate an onset temperature, and thus an activation energy, for the production of CO_m comparable to that observed with the IRAS spectra.

The PES C 1s lines allow an estimate of the probability of dehydrogenation of methanol on the Rh clusters. The C 1s intensity of methanol at 125 K (the point at 125 K in Figure 8b) reflects monolayer methanol on the surface, as the desorption signal for multilayer methanol is centered about 125 K (Figure 6) and that of CO_m at 300−350 K as the maximum production of CO_m (the point at either 300 or 350 K in Figure 8b). The latter is about 35% that of the former in Figure 8b. As for 3.0 ML Rh (cluster diameter >3.0 nm), the monolayer methanol was all on Rh clusters; the fraction 35% corresponded to a probability of methanol dehydrogenation on the Rh clusters. As a few CO_m molecules might have dissociated into elemental carbon at 300−350 K, 40−45% is a more reasonable estimate of the probability. For 0.5 ML Rh (cluster diameter <1.5 nm), the fraction 35% corresponds to a disparate probability. As the Rh surface area of 0.5 ML Rh clusters is only about 35% of that of 3.0 ML Rh clusters (according to STM measurements), the reactivity as the quantity of CO_m produced per surface Rh site must have been enhanced on the 0.5 ML Rh clusters. The STM images show that 0.5 ML Rh clusters shared about 40% of the total surface area of the sample (including both Rh and oxide surfaces). The fraction 35% implies that the probability of dehydrogenation of methanol on the 0.5 ML Rh clusters was more than double that on 3.0 ML Rh clusters.

DOI: 10.1021/acscatal.5b00579
ACS Catal. 2015, 5, 4276−4287

3.3. Mechanism of Decomposition of Methanol-d_4 from DFT Calculations. Figure 9 shows the modeled Rh nanocluster and surfaces. The Rh nanoclusters at the least coverage, 0.05 ML, in the experiment were modeled with a $\mathbf{Rh_{38}}$ cluster, a stable and spherically shaped structure of diameter ca. 0.9 nm. At greater coverages, the Rh clusters had apparently ordered structures, so were modeled with a Rh(100) surface. This surface was represented in a supercell comprising a 3 × 3 slab of five atomic layers, with the bottom two layers fixed and top three layers allowed to relax; an equivalent five-layer vacuum space was used to limit the artificial interaction between distinct adsorbates and slabs. The Rh(100) surfaces with lattice parameters optimized and increased 6% (denoted as **Rh(100)** and $\mathbf{Rh(100)_e}$ respectively) were modeled to simulate the 4.0 and 1.0 ML Rh clusters, respectively. The simulation did not include the Al_2O_3/NiAl(100) support because the interfacial interaction modified little the electronic structures of the supported Rh clusters. Our PES spectra show no dramatic BE shifts of Rh 3d, Al 2p, and O 1s levels due to a strong interface interaction (Supporting Information). The CO IRAS spectra show no oxidized Rh. Additionally, previous studies indicate that the role of the alumina support is marginal in catalyzed reactions.[86]

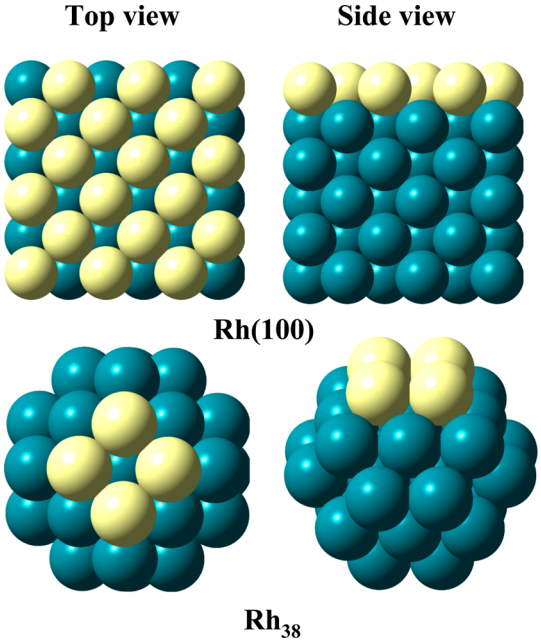

Figure 9. Top and side views of the **Rh(100)** surface and a $\mathbf{Rh_{38}}$ cluster in the computational models. The yellow spheres denote surface Rh atoms.

The decompositions of methanol-d_4 on **Rh(100)**, $\mathbf{Rh(100)_e}$, and $\mathbf{Rh_{38}}$ were all investigated to reveal the mechanism for the size-dependent behavior. The adsorption energy, E_{ads}, for CD_3OD* (the asterisk denoting adspecies) and its fragments on **Rh(100)**, $\mathbf{Rh(100)_e}$, and $\mathbf{Rh_{38}}$ was first examined, as shown in Figure 10. Figure 10a shows their optimized structures on **Rh(100)** and $\mathbf{Rh_{38}}$, for which only CD_3OD* preferred the atop site, whereas the other adspecies preferred the hollow or bridge sites. The structures on $\mathbf{Rh(100)_e}$ differ little from those on

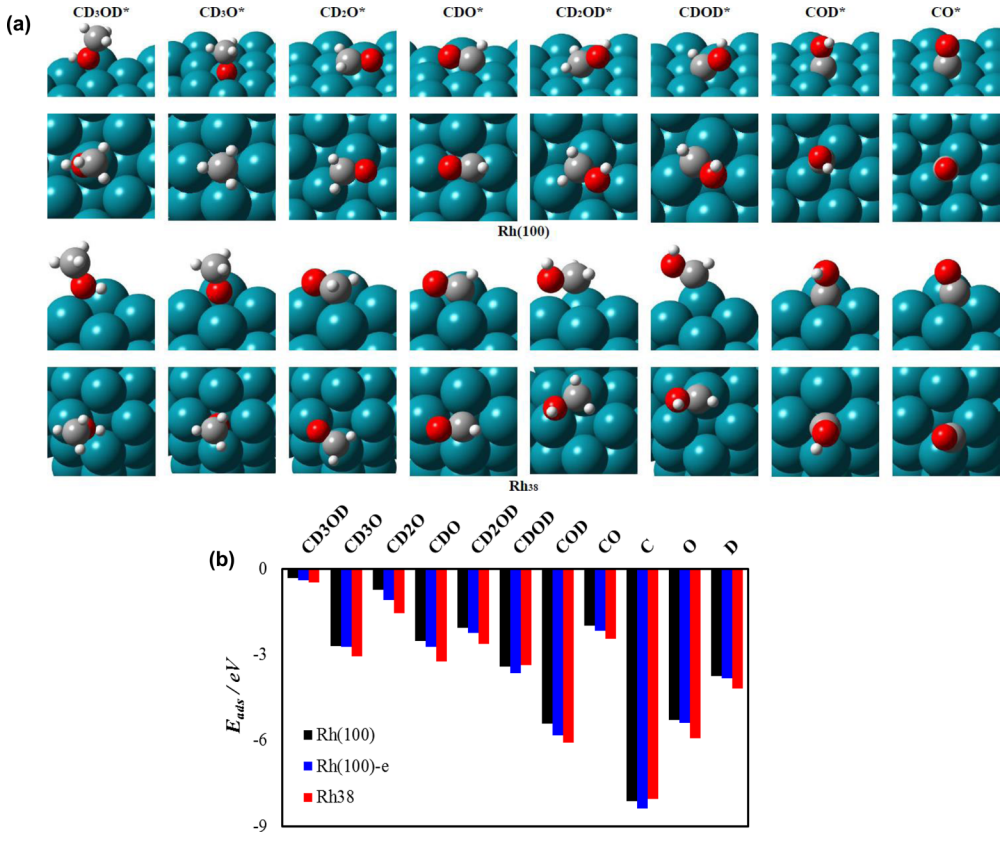

Figure 10. (a) Optimized structures of CD_3OD* and its decomposition fragments on **Rh(100)** and $\mathbf{Rh_{38}}$. (b) Comparison of E_{ads} on **Rh(100)**, $\mathbf{Rh(100)_e}$, and $\mathbf{Rh_{38}}$. In part a, gray, red, white, and cyan balls denote C, O, H, and Rh atoms, respectively.

DOI: 10.1021/acscatal.5b00579
ACS Catal. 2015, 5, 4276−4287

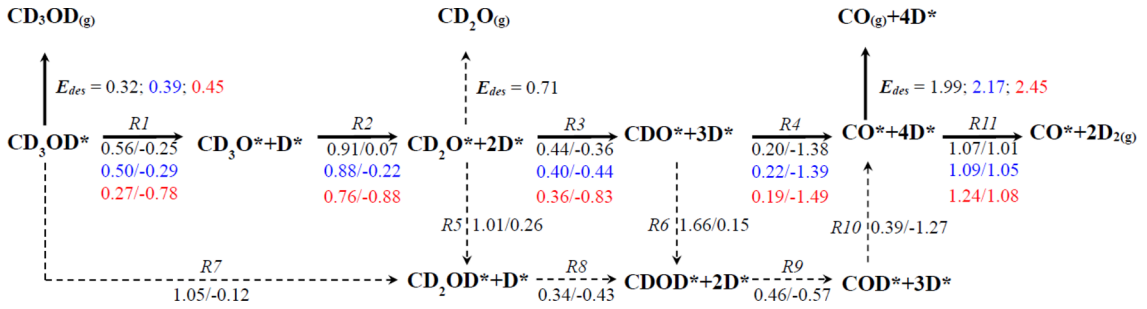

Figure 11. Schematic paths of CD_3OD decomposition. The energetically feasible path follows the thick arrows. $E_a/\Delta E$ values are given in the arrowed steps on **Rh(100)** in black, $\mathbf{Rh(100)_e}$ in blue, and $\mathbf{Rh_{38}}$ in red.

Rh(100) (not shown). Figure 10b shows a comparison of E_{ads} on the three surfaces; detailed data are given in Table S1 of the Supporting Information. **Rh(100)** had generally the smallest E_{ads}, whereas $\mathbf{Rh_{38}}$ had the greatest, which we attribute to the low-coordinated Rh atoms on the $\mathbf{Rh_{38}}$ surface having a higher d-band center[87] and being more active. The slightly increased E_{ads} value on $\mathbf{Rh(100)_e}$ corresponds to the expanded lattice. The E_{ads} analysis indicates that the desorption of molecularly adsorbed CO extended to higher temperature with decreasing cluster size (gray in Figure 5a). That E_{ads} varies with size is associated with the activity depending on size.

We simulated the CD_3OD decomposition on **Rh(100)**, $\mathbf{Rh(100)_e}$, and $\mathbf{Rh_{38}}$ to shed light on the energetics; the related structure for each step is presented in the Supporting Information. The reactive processes included a series of scissions of the O−D and C−D bonds of CD_3OD* to form CO_m* and D*, which yielded the ultimate products CO_m and D_2 observed in the TPD experiment. Scission of the C−O bond in CD_3OD* was not considered, as it was not observed and was unexpected theoretically.[88,89] We take the result from **Rh(100)** as an example to explain the computed energetics, schematically plotted in Figure 11. The most feasible path (marked in thick arrows) began with the scission of the O−D bond (*R1*) with a small activation energy (denoted as E_a), 0.56 eV, and proceeded with scissions of three consecutive C−D bonds (*R2*−*R4*). Among these steps, scission of the C−D bond of CD_3O* (*R2*) was the rate-determining step, having the greatest E_a, 0.91 eV. That E_a in *R2* was greater than E_a in *R1* implies that intermediate CD_3O* would accumulate and be observable on the surface.[34,35] The small E_a and exothermic energy (ΔE) in *R3* and *R4* ($E_a/\Delta E$ = 0.44/−0.36 and 0.20/−1.38 eV) indicate that the corresponding intermediates CD_2O* and CDO* have short lifetimes and thus become unobservable. These two E_a values are also smaller than those for the side hydrogenations *R5* and *R6* (1.01 and 1.66 eV) and than the desorption energy (E_{des}) for CD_2O* (0.71 eV). The alternative path began from scission of the C−D bond of CD_3OD* (*R7*) with E_a (1.05 eV) being much greater than that for *R1*. The resultant CD_2OD* could become further dehydrogenated through cleavage of its C−D bonds (*R8* and *R9*) with E_a values comparable to those of the similar dehydrogenation (*R3* and *R4*). The process ultimately directed to CO_m* and D* as well (*R10*), through breakage of the O−D bond and with a negligible barrier (0.07 eV).

The calculated energetics for the decomposition of CD_3OD agree with the experimental observations. Experiments on Rh(100) showed that CD_3O* appeared at 200−220 K but other intermediates, such as CD_2O* and CDO*, never existed in stable form on the surface.[35] Even molecularly adsorbed CD_2O* decomposed at 130 K.[34,82] Our IRAS spectra show consistently that only CD_3O* could exist in stable form on the Rh clusters. These observations conform to the most feasible path calculated above, in which CD_3OD* decomposed preferentially to CO_m* and D* via breakage of first the O−D bond (to form CD_3O*) and then C−D bonds. The simulation showed that the adspecies CO_m* and D* further stretched to the final products CO_m and D_2 on overcoming E_a = 1.07 eV for recombination of D* (*R11*) and E_{des} = 1.99 eV for desorption of CO_m*. Both energies were greater than any E_a value of decomposition steps *R1*−*R4*. The results are consistent with the present observations that CO_m* and D* appeared at temperatures 200−350 K whereas CO_m and D_2 appeared at >350 and >250 K, respectively. The results explain also that the onset temperature, 250 K, of desorption of D_2 is less than that of CO_m, 350 K.

To disclose the origin of the size-dependent behavior, we compared the calculated energetics along the energetically most favored path from $\mathbf{Rh(100)_e}$ (blue) and $\mathbf{Rh_{38}}$ (red) with those from **Rh(100)** (black). $\mathbf{Rh(100)_e}$ had a more exothermic ΔE value and decreased E_a in dehydrogenation steps *R1*−*R4* and a more endothermic ΔE value and increased E_a value in the association step *R11*. The energetic change is attributed to an increase in the lattice parameter, which narrows the metal d band and shifts up the antibonding band in the adsorption to strengthen E_{ads}, lower the bond dissociation E_a, and raise the bond association E_a.[90,91] $\mathbf{Rh_{38}}$ had the greatest energetic changes among the three Rh surfaces. The changes are attributed to the edge Rh atoms on top of $\mathbf{Rh_{38}}$ clusters (Figure 10a).[86,92−94] The dehydrogenation steps on the three Rh surfaces showed a similar trend: *R2* was the rate-determining step, with similar E_a values on the varied Rh surfaces. A similar energetic trend was indicated in previous work on other Rh facets, such as Rh(111) and Rh(211).[36,95] Both the reaction path and the rate-determining step are insensitive to the Rh surface structures. Although E_a on $\mathbf{Rh_{38}}$ was altered to some extent, the reaction path was not altered, as the large E_{ads} on $\mathbf{Rh_{38}}$ shifted the energetics analogously in all steps. This comparison supports our IRAS and PES measurements, according to which the formation of CO_m* and D* depended little on the cluster size. The large E_{ads} on $\mathbf{Rh_{38}}$ altered the competition between desorption and scission of the O−D bond of adsorbed methanol-d_4. On **Rh(100)**, E_a for scission of the O−D bond of CD_3OD* (*R1*, 0.56 eV) was greater than E_{des} (0.32 eV), leading to the preferential desorption of CD_3OD*. On $\mathbf{Rh(100)_e}$, the 6% increase of the lattice parameter changed the energetics but improved the activity little; CD_3OD* still preferred to desorb. The effect of the expanded lattice parameter is limited. Our experiments with

DOI: 10.1021/acscatal.5b00579
ACS Catal. 2015, 5, 4276−4287

1.0 ML or 4.0 ML Rh clusters support the result. In contrast, on $\mathbf{Rh_{38}}$, E_a in *R1* became smaller (0.27 eV) than E_{des} of CD_3OD* (0.45 eV), implying that most CD_3OD* proceeded toward dehydrogenation, instead of direct desorption. The varied activation energies opened the channel of dehydrogenation. The size-dependent activation energies for the scission of the O−D bond and desorption of methanol-d_4 are responsible for the enhanced productivity. According to our calculations of E_{ads} on $\mathbf{Rh_{38}}$ (Figure 10), these properties result from the edge Rh atoms at the surface of small clusters.

4. DISCUSSION

Focusing on the origin of the reactivity dependence on the size of the clusters, we find that several mechanisms might be responsible for the enhanced reactivity on small clusters. First, more methanol (or methanol-d_4) molecules adsorb per surface site on small clusters. Methanol could adsorb on small clusters with an increased concentration, but to a limited extent; the concentration on small clusters cannot be 2−4 times that on large clusters. Second, methanol adsorbed initially on uncovered Al_2O_3/NiAl(100) diffused to the Rh clusters to react. As the temperature of desorption of methanol on Al_2O_3/NiAl(100), at a maximum of about 190 K, was greater than that on Rh, centered at about 160 K, the methanol initially on the oxide might diffuse readily to unoccupied Rh sites at an elevated temperature. This mechanism nevertheless contradicts the negligible enhancement on 1.0 ML Rh clusters, which had apparently more oxide area than 4.0 ML Rh clusters/Al_2O_3/NiAl(100). Third, Rh clusters had a great density of defects such as step and corner sites, typically considered to serve as reactive sites. Earlier studies have shown that the low-coordinated Rh atoms at varied surfaces are reactive for CO dissociation.[86,92−94] Nevertheless, the role of ordinary defect sites on large clusters or single crystals is not essential in the present dehydrogenation. The density of defects is expected to increase with decreasing cluster size, whereas the reactivity of Rh clusters of diameter about 2.0 nm differs little from that at about 3.5 nm and also that of the Rh(100) surface (Figure 5b−d). Even an ion-sputtered Rh(100) surface, which had evidently more defects than a Rh(100) surface, showed limited enhancement in reactivity (see the Supporting Information). As a result, only the low-coordinated Rh sites on small clusters effectively enhance the production. On top edge sites of small clusters, the competition between desorption and scission of the O−D bond of adsorbed methanol-d_4 is altered.

When dehydrogenation became more favorable than desorption, for small clusters, the preceding first and second mechanisms likely contributed to the production, although either mechanism alone contributed little. We so argue because the production of CO_m and D_2 per surface site on small clusters is 2−4 times that on 4.0 ML Rh clusters; the probability of dehydrogenation of methanol on 4.0 ML Rh clusters or Rh(100) single crystal reaches 65% (or 40−45% on the basis of PES experiments).

5. CONCLUSION

With STM, RHEED, TPD, IRAS, synchrotron-based PES, and DFT calculations, we investigated the decomposition of methanol and methanol-d_4 on Rh clusters supported on an ordered thin film of Al_2O_3/NiAl(100) under UHV conditions. The Rh clusters were grown with vapor deposition onto the Al_2O_3/NiAl(100) surface at 300 K; their mean diameter evolved from 1.0 to 3.5 nm and their height from 0.4 to 0.8 nm with increasing coverage. The structure of clusters of diameter >1.5 nm became apparently ordered, having an fcc phase and growing in the (100) orientation; the lattice parameters of the clusters increased with decreasing cluster size, up to 6% with respect to bulk Rh. Methanol on Rh clusters decomposed via dehydrogenation to CO_m, which was significantly activated above 200 K, regardless of the cluster size. In contrast, the production of CO and hydrogen (deuterium) per Rh surface site varied notably with the cluster size. For Rh clusters of diameter <1.5 nm and height <0.6 nm, the production increased with decreasing size of the cluster; at a cluster diameter near 1.0 nm and height near 0.4 nm, the production of CO and hydrogen per Rh surface site is 4 times that on large clusters or the Rh(100) surface. The enhancement is attributed largely to a decreased E_a value for dehydrogenation to methoxy and increased E_{des} for methanol on the small clusters. We associate the varied energies with the edge Rh atoms at the surface of small clusters.

■ ASSOCIATED CONTENT

Supporting Information

The Supporting Information is available free of charge on the ACS Publications website at DOI: 10.1021/acscatal.5b00579.

Additional experimental data and DFT calculation results (PDF)

■ AUTHOR INFORMATION

Corresponding Authors

*E-mail for J.-H.W.: jenghan@ntnu.edu.tw.

*E-mail for M.-F.L.: mfl28@phy.ncu.edu.tw.

Notes

The authors declare no competing financial interest.

■ ACKNOWLEDGMENTS

The National Science Council provided support (NSC-100-2112-M-008-010-MY3 and NSC 101-2113-M-003-006-MY3) for this work. CPU time at Taiwan's National Center for High-performance Computing (NCHC) and the Department of Applied Chemistry in Private Chinese Culture University (PCCU) are greatly appreciated.

■ REFERENCES

(1) Hamnett, A. *Catal. Today* **1997**, *38*, 445−457.

(2) Williams, K. R.; Burstein, G. T. *Catal. Today* **1997**, *38*, 401−410.

(3) Burstein, G. T.; Barnett, C. J.; Kucernak, A. R.; Williams, K. R. *Catal. Today* **1997**, *38*, 425−437.

(4) Beden, B.; Lamy, C.; Leger, J. R. In *Electrocatalytic Oxidation of Oxygenated Aliphatic Organic Compounds at Noble Metal Electrodes*; Bockris, J. O. M., Conway, B. E., White, R. E., Eds.; Plenum Press: New York, 1992; Vol. *22*, p 566.

(5) Rostrup-Nielsen, J. R.; Nielsen, R. *Catal. Rev.: Sci. Eng.* **2004**, *46*, 247−270.

(6) Sexton, B. A. *Surf. Sci.* **1981**, *102*, 271−281.

(7) Sexton, B. A.; Hughes, A. E. *Surf. Sci.* **1984**, *140*, 227−248.

(8) Akhter, S.; White, J. M. *Surf. Sci.* **1986**, *167*, 101−126.

(9) Outka, D. A.; Madix, R. J. *J. Am. Chem. Soc.* **1987**, *109*, 1708−1714.

(10) Gibson, K. D.; Dubois, L. H. *Surf. Sci.* **1990**, *233*, 59−64.

(11) Wang, J.; Masel, R. I. *J. Am. Chem. Soc.* **1991**, *113*, 5850−5856.

(12) Kizhakevariam, N.; Stuve, E. M. *Surf. Sci.* **1993**, *286*, 246−260.

(13) Lazaga, M. A.; Wickham, D. T.; Parker, D. H.; Kastanas, G. N.; Koel, B. E. *Am. Chem. Soc. Symp. Ser.* **1993**, *523*, 90−109.

DOI: 10.1021/acscatal.5b00579
ACS Catal. 2015, 5, 4276−4287

(14) Chen, J.-J.; Jiang, Z.-C.; Zhou, Y.; Chakraborty, B. R.; Winograd, N. *Surf. Sci.* **1995**, *328*, 248−262.
(15) Francis, S. M.; Corneille, J.; Goodman, D. W.; Bowker, M. *Surf. Sci.* **1996**, *364*, 30−38.
(16) Huberty, J. S.; Madix, R. J. *Surf. Sci.* **1996**, *360*, 144−156.
(17) Zhang, C. J.; Hu, P. *J. Chem. Phys.* **2001**, *115*, 7182−7186.
(18) Ammon, C.; Bayer, A.; Held, G.; Richter, B.; Schmidt, T.; Steinrück, H.-P. *Surf. Sci.* **2002**, *507−510*, 845−850.
(19) Morkel, M.; Kaichev, V. V.; Rupprechter, G.; Freund, H.-J.; Prosvirin, I. P.; Bukhtiyarov, V. I. *J. Phys. Chem. B* **2004**, *108*, 12955−12961.
(20) Fuente, O. R. d. l.; Borasio, M.; Galletto, P.; Rupprechter, G.; Freund, H.-J. *Surf. Sci.* **2004**, *566−568*, 740−745.
(21) Vinod, C. P.; Niemantsverdriet, J. W.; Nieuwenhuys, B. E. *Phys. Chem. Chem. Phys.* **2005**, *7*, 1824−1829.
(22) Habermehl-Ćwirzeń, K.; Lahtinen, J.; Hautojärvi, P. *Surf. Sci.* **2005**, *598*, 128−135.
(23) Borasio, M.; Fuente, O. R. d. l.; Rupprechter, G.; Freund, H.-J. *J. Phys. Chem. B* **2005**, *109*, 17791−17794.
(24) Wang, G.-C.; Zhou, Y.-H.; Nakamura, J. *J. Chem. Phys.* **2005**, *122*, 044707.
(25) Matolínová, I.; Johánek, V.; Myslivecek, J.; Prince, K. C.; Skála, T.; Škoda, M.; Tsud, N.; Vorokhta, M.; Matolín, V. *Surf. Interface Anal.* **2011**, *43*, 1325−1331.
(26) Sheu, B.-R.; Chaturvedi, S.; Strongin, D. R. *J. Phys. Chem.* **1994**, *98*, 10258−10268.
(27) Panja, C.; Saliba, N.; Koel, B. E. *Surf. Sci.* **1998**, *395*, 248−259.
(28) Antolini, E.; Salgado, J. R. C.; Gonzalez, E. R. *Appl. Catal., B* **2006**, *63*, 137−149.
(29) Kim, K. S.; Barteau, M. A. *Surf. Sci.* **1989**, *223*, 13−32.
(30) Dilara, P. A.; Vohs, J. M. *Surf. Sci.* **1994**, *321*, 8−18.
(31) Mensch, M. W.; Byrd, C. M.; Cox, D. F. *Catal. Today* **2003**, *85*, 279−289.
(32) Mullins, D.; Robbins, M. D.; Zhou, J. *Surf. Sci.* **2006**, *600*, 1547−1558.
(33) Solymosi, F.; Berkó, A.; Tarnóczi, T. I. *Surf. Sci.* **1984**, *141*, 533−548.
(34) Houtman, C.; Barteau, M. A. *Langmuir* **1990**, *6*, 1558−1566.
(35) Parmeter, J. E.; Jiang, X.; Goodman, D. W. *Surf. Sci.* **1990**, *240*, 85−100.
(36) Jiang, R.; Guo, W.; Li, M.; Zhu, H.; Zhao, L.; Lu, X.; Shan, H. *J. Mol. Catal. A: Chem.* **2011**, *344*, 99−110.
(37) Zhou, J.; Mullins, D. R. *J. Phys. Chem. B* **2006**, *110*, 15994−16002.
(38) Schauermann, S.; Hoffmann, J.; Johánek, V.; Hartmann, J.; Libuda, J. *Phys. Chem. Chem. Phys.* **2002**, *4*, 3909−3918.
(39) Bäumer, M.; Libuda, J.; Neyman, K. M.; Rösch, N.; Rupprechter, G.; Freund, H.-J. *Phys. Chem. Chem. Phys.* **2007**, *9*, 3541−3558.
(40) Chao, C.-S.; Li, Y.-D.; Hsu, B.-W.; Lin, W.-R.; Hsu, H.-C.; Hung, T.-C.; Wang, C.-C.; Luo, M.-F. *J. Phys. Chem. C* **2013**, *117*, 5667−5677.
(41) Nehasil, V.; Stará, I.; Matolín, V. *Surf. Sci.* **1995**, *331−333*, 105−109.
(42) Frank, M.; Andersson, S.; Libuda, J.; Stempel, S.; Sandell, A.; Brena, B.; Giertz, A.; Brühwiler, P. A.; Bäumer, M.; Mårtensson, N.; Freund, H.-J. *Chem. Phys. Lett.* **1997**, *279*, 92−99.
(43) Andersson, S.; Frank, M.; Sandell, A.; Giertz, A.; Brena, B.; Brühwiler, P. A.; Mårtensson, N.; Libuda, J.; Bäumer, M.; Freund, H.-J. *J. Chem. Phys.* **1998**, *108*, 2967−2974.
(44) Gassmann, P.; Franchy, R.; Ibach, H. *Surf. Sci.* **1994**, *319*, 95−109.
(45) Blum, R.; Ahlbehrendt, D.; Niehus, H. *Surf. Sci.* **1998**, *396*, 176−188.
(46) Frémy, N.; Maurice, V.; Marcus, P. *J. Am. Ceram. Soc.* **2003**, *86*, 669−675.
(47) Zei, M. S.; Lin, C. S.; Wei, W. H.; Chiang, C. I.; Luo, M. F. *Surf. Sci.* **2006**, *600*, 1942−1951.
(48) Luo, M. F.; Chiang, C. I.; Shiu, H. W.; Sartale, S. D.; Kuo, C. C. *Nanotechnology* **2006**, *17*, 360−366.
(49) Luo, M. F.; Wen, W. H.; Lin, C. S.; Chiang, C. I.; Sartale, S. D.; Zei, M. S. *Surf. Sci.* **2007**, *601*, 2139−2146.
(50) Hong, I.-H.; Lee, T.-H.; Yin, G.-C.; Wei, D.-H.; Juang, J.-M.; Dann, T.-E.; Klauser, R.; Chuang, T. J.; Chen, C. T.; Tsang, K.-L. *Nucl. Instrum. Methods Phys. Res., Sect. A* **2001**, *467*, 905−908.
(51) Maurice, V.; Frèmy, N.; Marcus, P. *Surf. Sci.* **2005**, *581*, 88−104.
(52) Moulder, J. F.; Stickle, W. F.; Sobol, P. E.; Bomben, K. D. *Handbook of X-ray Photoelectron Spectroscopy*; Physical Electronics: Eden Prairie, MN, 1995; p 54.
(53) Sartale, S. D.; Shiu, H. W.; Tien, M. H.; Chiang, C. I.; Luo, M. F.; Lin, Y. C.; Hsu, Y. J. *J. Phys. Chem. C* **2008**, *112*, 2066−2073.
(54) Kresse, G.; Furthmüller, J. *Phys. Rev. B: Condens. Matter Mater. Phys.* **1996**, *54*, 11169−11186.
(55) Kresse, G.; Hafner, J. *Phys. Rev. B: Condens. Matter Mater. Phys.* **1993**, *47*, 558−561.
(56) Kresse, G.; Hafner, J. *Phys. Rev. B: Condens. Matter Mater. Phys.* **1994**, *49*, 14251−14269.
(57) Ceperley, D. M.; Alder, B. J. *Phys. Rev. Lett.* **1980**, *45*, 566−569.
(58) Perdew, J. P.; Wang, Y. *Phys. Rev. B: Condens. Matter Mater. Phys.* **1992**, *45*, 13244−13249.
(59) Blöchl, P. E. *Phys. Rev. B: Condens. Matter Mater. Phys.* **1994**, *50*, 17953−17979.
(60) Kresse, G.; Joubert, D. *Phys. Rev. B: Condens. Matter Mater. Phys.* **1999**, *59*, 1758−1775.
(61) Monkhorst, H. J.; Pack, J. D. *Phys. Rev. B* **1976**, *13*, 5188−5192.
(62) Mills, G.; Jonsson, H.; Schenter, G. K. *Surf. Sci.* **1995**, *324*, 305−337.
(63) Luo, M. F.; Shiu, H. W.; Tien, M. H.; Sartale, S. D.; Chiang, C. I.; Lin, Y. C.; Hsu, Y. J. *Surf. Sci.* **2008**, *602*, 241−248.
(64) Bäumer, M.; Frank, M.; Heemeier, M.; Kühnemuth, R.; Stempel, S.; Freund, H.-J. *Surf. Sci.* **2000**, *454−456*, 957−962.
(65) Luo, M. F.; Wen, W. H.; Lin, C. S.; Chiang, C. I.; Sartale, S. D.; Zei, M. S. *Surf. Sci.* **2007**, *601*, 2139−2146.
(66) Luo, M. F.; Ten, M. H.; Wang, C. C.; Lin, W. R.; Ho, C. Y.; Chang, B. W.; Wang, C. T.; Lin, Y. C.; Hsu, Y. J. *J. Phys. Chem. C* **2009**, *113*, 12419−12426.
(67) Luo, M. F.; Wang, C. C.; Hu, G. R.; Lin, W. R.; Ho, C. Y.; Lin, Y. C.; Hsu, Y. J. *J. Phys. Chem. C* **2009**, *113*, 21054−21062.
(68) Cavallin, A.; Pozzo, M.; Africh, C.; Baraldi, A.; Vesselli, E.; Dri, C.; Comelli, G.; Larciprete, R.; Lizzit, S.; Alfè, D. *ACS Nano* **2012**, *6*, 3034−3043.
(69) Hu, G.-R.; Chao, C.-S.; Shiu, H.-W.; Wang, C.-T.; Lin, W.-R.; Hus, Y.-J.; Luo, M.-F. *Phys. Chem. Chem. Phys.* **2011**, *13*, 3281−3290.
(70) Stubenrauch, J.; Vohs, J. M. *Catal. Lett.* **1997**, *47*, 21−25.
(71) Putna, E. S.; Gorte, R. J.; Vohs, J. M.; Graham, G. M. *J. Catal.* **1998**, *178*, 598−603.
(72) CO on Rh(100) single crystal does not occupy each Rh atop site,[73] and the occupancy rates for CO on Rh single crystal and Rh clusters could differ.
(73) Jansen, M. M. M.; Gracia, J.; Nieuwenhuys, B. E.; Niemantsverdriet, J. W. *Phys. Chem. Chem. Phys.* **2009**, *11*, 10009−10013.
(74) The ionization cross-section for varied species and at varied partial pressure has been considered.
(75) The dissociation rate for CO on Rh clusters depends on the cluster size. Earlier studies show the rate varied between 0.25 and 0.5.[43] Our PES experiments showed a comparable result in our system (see the Supporting Information): 0.55 for 3 ML and 0.21 for 0.25 ML Rh.
(76) Frank, M.; Kühnemuth, R.; Bäumer, M.; Freund, H.-J. *Surf. Sci.* **1999**, *427−428*, 288−293.
(77) Krenn, G.; Bako, I.; Schennach, R. *J. Chem. Phys.* **2006**, *124*, 144703.
(78) Koch, H. P.; Singnurkar, P.; Schennach, R.; Stroppa, A.; Mittendorfer, F. *J. Phys. Chem. C* **2008**, *112*, 806−812.
(79) Hadjiivanov, K. I. *J. Chem. Soc., Faraday Trans.* **1998**, *94*, 1901−1904.

DOI: 10.1021/acscatal.5b00579
ACS Catal. 2015, 5, 4276−4287

(80) Happel, M.; Mysliveček, J.; Johánek, V.; Dvořák, F.; Stetsovych, O.; Lykhach, Y.; Matolín, V.; Libuda, J. *J. Catal.* **2012**, *289*, 118−126.
(81) Chakarova, K.; Hadjiivanov, K.; Atanasova, G.; Tenchev, K. *J. Mol. Catal. A: Chem.* **2007**, *264*, 270−279.
(82) Houtman, C.; Barteau, M. A. *Surf. Sci.* **1991**, *248*, 57−76.
(83) Lee, S. H.; Ishizaki, T.; Saito, N.; Takai, O. *Surf. Sci.* **2007**, *601*, 4206−4211.
(84) Kim, M. K.; Baik, J.; Jeon, C.; Song, I.; Nam, J. H.; Hwang, H.-N.; Hwang, C. C.; Woo, S. H.; Park, C.-Y.; Ahn, J. R. *Surf. Sci.* **2010**, *604*, 1598−1602.
(85) Makowski, M. S.; Zemlyanov, D. Y.; Lindsey, J. A.; Bernhard, J. C.; Hagen, E. M.; Chan, B. K.; Petersohn, A. A.; Medow, M. R.; Wendel, L. E.; Chen, D.; Canter, J. M.; Ivanisevi, A. *Surf. Sci.* **2011**, *605*, 1466−1475.
(86) de Mongeot, B. F.; Toma, A.; Molle, A.; Lizzit, S.; Petaccia, L.; Baraldi, A. *Phys. Rev. Lett.* **2006**, *97*, 056103.
(87) Pushpa, R.; Ghosh, P.; Narasimhan, S.; Gironcoli, S. d. *Phys. Rev. B: Condens. Matter Mater. Phys.* **2009**, *79*, 165406.
(88) Stroppa, A.; Mittendorfer, F.; Andersen, J. N.; Parteder, G.; Allegretti, F.; Surnev, S.; Netzer, F. P. *J. Phys. Chem. C* **2009**, *113*, 942−949.
(89) Zhao, X.; Zhang, R.; Ling, L.; Wang, B. *Appl. Surf. Sci.* **2014**, *320*, 681−688.
(90) Huang, S.-C.; Lin, C.-H.; Wang, J. H. *J. Phys. Chem. C* **2010**, *114*, 9826−9834.
(91) Lin, C.-H.; Chen, C.-L.; Wang, J.-H. *J. Phys. Chem. C* **2011**, *115*, 18582−18588.
(92) Mavrikakis, M.; Bäumer, M.; Freund, H.-J.; Nørskov, J. K. *Catal. Lett.* **2002**, *81*, 153−156.
(93) Rebholz, M.; Prins, R.; Kruse, N. *Surf. Sci.* **1991**, *259*, L797−L803.
(94) Ertl, G.; Freund, H.-J. *Phys. Today* **1999**, *52*, 32−40.
(95) Kapur, N.; Hyun, J.; Shan, B.; Nicholas, J. B.; Cho, K. *J. Phys. Chem. C* **2010**, *114*, 10171−10182.

DOI: 10.1021/acscatal.5b00579
ACS Catal. 2015, 5, 4276−4287